

A Comprehensive Analysis of *Fermi* Gamma-ray Burst Data: III. Energy-Dependent T_{90} Distributions of GBM GRBs and Instrumental Selection Effect on Duration Classification

Ying Qin¹, En-Wei Liang^{1,2,3}, Yun-Feng Liang¹, Shuang-Xi Yi⁴, Lin Lin⁵, Bin-Bin Zhang⁶,
Jin Zhang^{2,7}, Hou-Jun Lü³, Rui-Jing Lu¹, Lian-Zhong Lü¹, and Bing Zhang³

ABSTRACT

The durations (T_{90}) of 315 GRBs detected with *Fermi*/GBM (8-1000 keV) by 2011 September are calculated using the Bayesian Block method. We compare the T_{90} distributions between this sample and those derived from previous/current GRB missions. We show that the T_{90} distribution of this GRB sample is bimodal, with a statistical significance level being comparable to those derived from the *BeppoSAX*/GRBM sample and the *Swift*/BAT sample, but lower than that derived from the *CGRO*/BATSE sample. The short-to-long GRB number ratio is also much lower than that derived from the BATSE sample, i.e., 1:6.5 vs 1:3. We measure T_{90} in several bands, i.e., 8-15, 15-25, 25-50, 50-100, 100-350, and 350-1000 keV, to investigate the energy-dependence effect of the bimodal T_{90} distribution. It is found that the bimodal feature is well observed in the 50-100 and 100-350 keV bands, but is only marginally acceptable in the 25-50 keV and 350-1000 keV bands. The hypothesis of the bimodality is confidently rejected in the 8-15 and 15-25 keV bands. The T_{90} distributions in these bands are roughly consistent with those observed by missions with similar energy bands. The parameter T_{90} as a function of energy follows $\bar{T}_{90} \propto E^{-0.20 \pm 0.02}$ for long GRBs.

¹Department of Physics and GXU-NAOC Center for Astrophysics and Space Sciences, Guangxi University, Nanning 530004, China; lew@gxu.edu.cn

²The National Astronomical Observatories, Chinese Academy of Sciences, Beijing 100012, China

³Department of Physics and Astronomy, University of Nevada, Las Vegas, NV 89154; zhang@physics.unlv.edu

⁴College of Astronomy and Space Sciences, Nanjing University, Nanjing, 210093, China

⁵Sabancı University, Faculty of Engineering and Natural Sciences, Orhanlı– Tuzla, İstanbul 34956, Turkey

⁶Department of Astronomy and Astrophysics, Pennsylvania State University, University Park, PA 16802, USA

⁷College of Physics and Electronic Engineering, Guangxi Teachers Education University, Nanning, 530001, China

Considering the erratic X-ray and optical flares, the duration of a burst would be even much longer for most GRBs. Our results, together with the observed extended emission of some short GRBs, indicate that the central engine activity time scale would be much longer than T_{90} for both long and short GRBs and the observed bimodal T_{90} distribution may be due to an instrumental selection effect.

Subject headings: gamma-rays: bursts – methods: statistics

1. Introduction

The gamma-ray burst (GRB) survey with Burst And Transient Source Experiment (BATSE) on board Compton Gamma-Ray Observatory (CGRO) revealed a clear bimodal distribution of the burst duration parameter T_{90} , which is measured with the time interval from 5% to 95% accumulative photon counts from the source, and two groups of GRBs, i.e., long vs. short GRBs with a division line at $T_{90} = 2$ seconds, was identified (Kouveliotou et al. 1993). It has been long theoretically speculated that long GRBs (LGRBs) are related to the deaths of massive stars (Colgate 1974; Woosley 1993). This is observationally confirmed with the discoveries of the supernovae (SNe) association with some nearby LGRBs (for reviews, see Zhang & Mészáros 2004; Piran 2005; Mészáros 2006; Woosley & Bloom 2006). The rapid localization capacity of the *Swift* GRB mission (Gehrels et al. 2004) led to redshift measurements and host galaxy detections of short GRBs (SGRBs). Some nearby SGRBs are found in elliptical/early-type galaxies with very low star formation rates (Gehrels et al. 2005; Bloom et al. 2006; Barthelmy et al. 2005a; Berger et al. 2005) or in the regions with a low star formation rate in star-forming galaxies (Covino et al. 2006; Fox et al. 2005). These are consistent with a non-massive star origin of SGRBs, probably related to the mergers of two compact objects (e.g., Paczyński 1986, 1991; Eichler et al. 1989; Narayan et al. 1992; Bloom et al. 1999; see Nakar 2007 for a review). The SGRB central engine in this model is a hot and dense torus of $0.01 \sim 0.3 M_{\odot}$ that is accreted onto a stellar mass black hole. The life time of a SGRB is expected to be typically shorter than 2 seconds (Popham, Woosley & Fryer, 1999; Narayan, Piran & Kumar, 2001; Di Matteo, Perna & Narayan, 2002). This is roughly consistent with the typical T_{90} s of SGRBs observed with BATSE.

It was surprising that two nearby LGRBs, i.e. GRB 060614 ($T_{90} = 103$ seconds at $z = 0.125$) and 060605 ($T_{90} = 4$ seconds at $z = 0.089$), had no detection of an accompanied SN, different from other known nearby LGRBs, such as GRB 980425/SN 1998bw (Galama et al. 1998; Kulkarni et al. 1998), GRB 030329/SN 2003dh (Stanek et al. 2003; Hjorth et al. 2003), GRB 031203/SN 2003lw (Malesani et al. 2004), GRB 060218/SN 2006aj (Modjaz

et al. 2006; Pian et al. 2006; Sollerman et al. 2006; Mirabal et al. 2006; Cobb et al. 2006), and 100316D/SN 2010bh (Starling et al. 2011; Fan et al. 2011). The prompt emission and afterglow properties of GRB 060614 are similar to those of some nearby “short” GRBs that have a non-massive star origin (e.g. Gehrels et al. 2006; Zhang et al. 2007; Gal-Yam et al. 2006). This led to confusion of the long-short classification scheme and a new classification scheme, i.e. Type II (massive star origin) vs. Type I (compact star origin) was proposed (Zhang 2006; Zhang et al. 2007). Note that some well-known Type I GRBs, such as GRB 050724 (Barthelmy et al. 2005; Tanvir et al. 2005; Berger et al. 2005) and 050709 (Hjorth et al. 2005; Villasenor et al. 2005; Fox et al. 2005) also have a long-lasting extended emission component, making T_{90} of these bursts to be ~ 100 seconds. In fact, a handful of Type I GRBs show such a component in their lightcurves (Norris et al. 2008; Lin et al. 2008; Zhang et al. 2009). GRB 060614-like nearby LGRBs are therefore likely Type I GRBs with a long, soft extended emission tail, similar to that observed in SGRB 050724 (Zhang et al. 2007). It is also interesting to note that some short-duration GRBs are likely originated from collapse of massive stars (Virgili et al. 2011; Zhang et al. 2009), such as GRB 090426 ($T_{90} = 1.28$ in the 15-350 keV band; Levesque et al. 2010a, b; Xin et al. 2010). Some high redshift GRBs, such as GRBs 080913 ($z = 6.7$; Greiner et al. 2009) and 090423 ($z = 8.3$; Salvaterra et al. 2009; Tanvir et al. 2009), have a rest-frame short duration ($T_{90}/(1+z) < 2$ seconds), but they share a lot of common properties with LGRBs, and are likely from collapse of massive stars (Zhang et al. 2009; Belczynski et al. 2010; Levesque et al. 2010a; Lin et al. 2010). These observations indicate that the long vs. short GRB classification scheme does not always match the physical Type II vs. Type I classification scheme. Lü et al. (2010) proposed a new observational parameter defined with the burst isotropic gamma-ray energy and the photon energy of the νf_ν spectral peak (E_p). Similarly, the ratio of the gamma-ray fluence to E_p is also suggested as a parameter for GRB classification (Goldstein et al. 2010).

As discussed above, T_{90} is not always a good parameter to conduct GRB classification. It is essential to understand whether the observed bimodal T_{90} distribution is intrinsic or just due to an instrumental selection effect. This is critical for GRB classification and theoretical modeling of GRB progenitors and central engines. Broadband energy band observations with the *Fermi* mission not only reveal the spectral components and their temporal evolution (Zhang et al. 2011, Lu et al. 2012; Paper I and II of this series), but also provide an opportunity to study the energy dependence of burst duration and possible instrumental selection effect on the T_{90} distribution. In this paper, we present a detailed analysis on the T_{90} distribution of *Fermi*/GBM sample (in Section 2), and compare it with the T_{90} distributions derived from the previous GRB missions (in Section 3). We next explore the instrumental selection effect on T_{90} distribution and energy dependence of T_{90} (in Section 4). We also present discussion on the burst duration by considering late X-ray and optical flares

(in Section 5). We show that the bimodal distribution of T_{90} is likely due to an instrumental selection effect and the life time of the central engines of Type I GRBs is essentially longer than 2 seconds for most cases (in Section 6).

2. Data Reduction and Calculation of T_{90}

We include all 315 GRBs detected by GBM, as reported by the GBM team in GCN circulars up to Sep. 2011. We download the data from *Fermi* Archive available at *ftp://legacy.gsfc.nasa.gov/f*. The time tagged event (TTE) data have excellent time resolution of $2\mu\text{s}$. The TTE data of the most illuminated NaI detector for each GRB is used for our analysis. The Rmfit(v3.7) package is used for data reduction.

We select two time intervals that are far before and far after the main burst as background and extract it during the burst phase by a linear fit¹, then calculate T_{90} using the Bayesian Block method (Scargle et al. 1998). Note that we do not adopt fixed intervals prior to or post the GRB trigger as the background, since some GRBs have significant emission prior to the trigger, while some others may have a long tail after the main burst. Therefore, the background intervals were visually selected by eye for each GRB. The background subtraction of the lightcurve alters the prior assumption used in the Bayesian Block method and adds additional error into the duration estimation due to the propagation of error from the background. However, it is found that this effect does not significantly affect our T_{90} estimation within error. To clarify the influence of interval selection for background subtraction in our calculation of T_{90} , we compare the derived T_{90} by selecting different background intervals for three typical GRBs. The lightcurves and selection of background intervals of these GRBs are displayed in Figure 1. For GRB 091010, a bright burst, the derived T_{90} values are 7.616 ± 0.580 s and 7.552 ± 0.516 for two different selections of the time intervals for background subtraction, as shown in Figure 1. For GRB 090126B, a weak burst, we get 8.032 ± 1.154 s and 7.968 ± 1.111 s, respectively. For GRB 090227B, a short GRB, we get 1.248 ± 0.601 s and 1.184 ± 0.544 s, respectively. One can find that the derived T_{90} values are consistent with each other within error for different background selections.

For each GRB in our sample, we extract the 64-ms binned light curves from the TTE data and subtract background for each energy band. We then calculate T_{90} with the Bayesian Block method (Scargle et al. 1998) for each lightcurve. Examples of lightcurve structure obtained from this method are also shown in Figure 1. With this method, we derive the

¹Higher order polynomial fits for background subtraction was also tried, but the derived T_{90} is generally consistent with that derived from the linear fit within error.

epochs of t_5 and t_{95} , where t_5 and t_{95} are the times when 5% and 95% of the total count fluence are collected, respectively². In order to reduce fluctuation of t_5 and t_{95} from a real lightcurve and estimate their error, we generate a sample of 10^3 mock lightcurve assuming that the error of lightcurve data has a Poisson distribution. The t_5 and t_{95} values as well as their errors (1σ) are obtained from a Gaussian fit to their distributions from the mock lightcurve sample. Hence, we get $T_{90} = t_{95} - t_5$ and its error $\delta T_{90} = (\delta t_{95}^2 + \delta t_5^2)^{1/2}$. The derived T_{90} are reported in Table 1³. Note that some lightcurves are too weak to calculate the values of t_5 and t_{95} with the Bayesian Block method. Therefore, their T_{90} values are not available.

The T_{90} reported in Fermi GBM Catalog by the GBM team is calculated by accumulating the photon fluence through the duration of the burst (Paciesas et al. 2012). In this method, a GRB is split into some time bins and the spectrum of each bin is fit with a model. The photon fluence from the best fit spectral model for each time bin is accumulated to calculate the T_{90} . This procedure factors in the detector response and the fact that the angle between the detectors and source are constantly changing. Figure 2 compares the derived T_{90} in the 50-300 keV band from the the Bayesian Block method with that derived from the the photon fluence method as reported by Paciesas et al. (2012). It is found that they are generally consistent with each other.

3. Comparison of the T_{90} Distribution to Other GRB Missions

Since 1990, GRB surveys in different energy bands have been done with *CGRO*/BATSE (50-300 keV), *HETE-2*/FREGATE (6-80 keV), *BeppoSAX*/GRBM (40-700 keV), *Swift*/BAT (15-150 keV), and *INTEGRAL*/SPI-ACS (20 keV-8 MeV). The GBM roughly covers the energy bands of these instruments. In Figure 3 and Table 2, we compare the T_{90} distribution of our GBM sample in the 8-1000 keV band with those derived from the data collected by these missions. The data of *HETE-2*/FREGATE, *BeppoSAX*/GRBM, *CGRO*/BATSE, *Swift*/BAT, *INTEGRAL*/SPI-ACS, are taken from Pélangeon et al. (2008), Frontera et al. (2009), Paciesas et al. (1999), Sakamoto et al. (2011), and Savchenko et al. (2012) respectively. Notice that the methods of T_{90} calculations adopted by these instrumental teams may not be exactly the same. In the *BeppoSAX*, *HETE-2*, *CGRO*/BATSE and *Integral* samples, the T_{90} values were derived by using the accumulated count rate. The T_{90} values

²Our calculation is done purely in count space. Since GBM is constantly slewing in orbit, this method could skew the T_{90} estimation of long GRBs.

³Table 1 is available only in the electronic version

of the *Swift* GRB sample were calculated using the Bayesian block method. The T_{90} values of *Fermi* GRBs reported by *Fermi* GBM team are calculated with the the photon fluence method by considering the instrument response effect, as described in §2. The derived T_{90} values with different methods for these instruments may have a small systematic bias, which does not greatly affect our comparison of the T_{90} distributions in our analysis.

As shown in Figure 3, the T_{90} distributions of the LGRB groups observed with different missions are generally consistent with each other, but those of the SGRBs are dramatically different. The *HETE-2* sample even does not have any GRB with $T_{90} < 2$ seconds. We fit the T_{90} distributions with a model of two log-normal functions and find that the bimodal distribution feature is revealed only in the BATSE, GBM, *BeppoSAX* and *INTEGRAL* samples. For the BATSE sample, the T_{90} distribution peaks at $\log T_{90} = -0.02 \pm 0.73$ and $\log T_{90} = 1.57 \pm 0.41$. For the GBM sample, the peaks are at $\log T_{90} = -0.27 \pm 0.28$ and $\log T_{90} = 1.32 \pm 0.49$, respectively. For the *BeppoSAX* sample, the peaks are at $\log T_{90} = 0.27 \pm 0.41$ and $\log T_{90} = 1.41 \pm 0.40$, respectively. For the *INTEGRAL* sample, the peaks are at $\log T_{90} = -0.29 \pm 0.06$ and $\log T_{90} = 1.36 \pm 0.01$, respectively. For the *Swift*/BAT sample, two Gaussian components are fit to the data, i.e., $\log T_{90} = -0.45 \pm 0.14$ and $\log T_{90} = 1.66 \pm 0.03$. For the *HETE-2* sample, one gets $\log T_{90} = 1.36 \pm 0.50$. Apparently, the bimodal feature is observed only in the *CGRO*/BATSE and *Fermi*/GBM-NaI samples, and it is consistent with the result of Zhang et al. (2012), who measure T_{90} with the observed fluence. The short-to-long GRB number ratios are also dramatically different, as reported in Table 2. In the *HETE-2*/FREGATE sample, no GRB with $T_{90} < 2$ seconds was detected ⁴. The short-to-long GRB ratios in the *Swift*/BAT, *BeppoSAX*/GRBM and *INTEGRAL*/SPI-ACS samples are 51:557 (1:11), 111:892 (1:8), and 195:724 (1:3.7), respectively. This ratio becomes 39:253 (1:6.5) in the GBM sample and 500:1541 (1:3) in the *CGRO*/BATSE sample.

Since the visible bimodal distribution feature depends on the bin size selection, we further test the bimodality of the T_{90} distribution with the KMM algorithm (Ashman et al. 1994), which is a Gaussian mixture model with parameters estimated by maximum likelihood estimation using the Expectation-Maximization algorithm. This algorithm has been widely used for population and classification studies by astronomers (e.g., Knigge et al. 2011; Lü et al. 2010). The details of the mixture modeling approach and clustering analysis was presented in McLachlan & Basford (1988) and McLachlan & Peel (2000). We use the

⁴Some *HETE-2* GRBs are possibly associated with short GRBs in the BATSE band. However, their T_{90} are essentially long in the *HETE-2* band. There include GRBs 020531 (~ 2 s in 2-10 keV; Lamb et al. 2003), 040802 ($T_{90} = 3.05 \pm 0.18$ in 6-80 keV), 050709 (143 s in 15-150 keV; Barthelmy et al. 2005), 051211 ($T_{90} = 4.9 \pm 0.61$; Pélagéon et al. 2008), and 060121 ($T_{90} = 2.6 \pm 0.1$; Pélagéon et al. 2008).

code by Ashman et al. (1994) who applied this technique for detecting and measuring the bimodality of astronomical data sets. The resulting significance of bimodality from the code is a P-value (P^{KMM}) and a likelihood ratio of 1 vs 2 Gaussians. The P-value represents the probability of determining the likelihood ratio test statistics from a distribution drawn from a single Gaussian. Notice that the ratio of the likelihood may not be useful without also considering the increased number of parameters in the latter model. Thus, it is most common to use penalized likelihood ratio tests such as the the Bayesian information criterion (Schwarz et al. 1978) rather than the classical likelihood ratio test. As a result, we only report the p^{KMM} values. A small P^{KMM} rejects the one single Gaussian distribution for the data with higher confidence. Conventionally, $P^{\text{KMM}} < 0.05$ rejects one Gaussian component in the data. We report the p^{KMM} values for the T_{90} distributions of these instruments in Table 3. The significance level of the bimodal feature in the GBM-NaI sample is comparable to that of the *BeppoSAX*/GRBM and *Swift*/BAT samples, but is much lower than the *CGRO*/BATSE sample. The hypothesis of a bimodal T_{90} distribution for the HETE-2 sample is confidently rejected.

It is also found that the spectra of SGRBs tend to be harder than LGRBs, where the spectral hardness ratio (HR) is defined with the fluence ratio between in the 100-350 keV band to that in the 25-50 keV band of BATSE (Kouveliotou et al. 1993). The GBM-NaI energy band covers a similar energy band as that of BATSE, but extends to a lower energy band. Therefore, we also derive the observed fluence in the two energy bands with the spectral parameters reported in GCN circulars for GBM GRBs in our sample, and examine the long-soft vs short-hard classification scheme. Figure 4 shows the comparison of the GRBs in our sample with the BATSE GRB sample in the $HR - T_{90}$ plane. One can observe that they are consistent with each other.

4. Energy Dependence of T_{90}

As shown above, the T_{90} distribution is instrument-dependent. The deficit of SGRBs in samples observed with instruments in a lower energy band, such as *HETE-2*/FREGATE and *Swift*/BAT, may be understood as combination of the following two effects. First, since SGRBs are typically harder, one has a lower trigger probability with a soft instrument. Second, many SGRBs have longer softer tails, which are readily detectable in softer detectors. As a result, some GRBs that would be classified as "short" are detected as "long" in soft detectors. As seen in GRB 050724 and 050709, the T_{90} of Type I GRBs is energy-dependent and it could be much longer than 2 seconds. In this section, we investigate the energy dependence of T_{90} with the GBM data. We derive the T_{90} values in the following energy

bands: 8-15 keV, 15-25 keV, 25-50 keV, 50-100 keV, 100-350 keV and 350-1000 keV. The short-to-long number ratios in each energy band are also reported in Table 2. The T_{90} distributions are shown in Figure 5. Comparing the T_{90} distributions with those observed by other instruments with similar energy bands, it is found that they are roughly consistent with each other, i.e., 8-15 keV band vs. *HETE-2*/FREGATE (6-80 keV), 15-25 and 25-50 keV bands vs. *Swift*/BAT (15-150 keV), 50-100 KeV band vs. *BeppoSAX*/GRBM (40-700 keV), and 100-350 band vs. *CGRO*/BATSE (25-2000 keV). We also try to fit the T_{90} distributions with the two log-normal component models. Similar results as shown in Figure 3 are obtained. The most significant bimodal T_{90} distribution is seen in the 100-350 keV band. We examine the bimodal feature in the T_{90} distributions of these energy bands with the KMM algorithm and our results are also reported in Table 2. It is found that the bimodal hypothesis is rejected for the T_{90} distributions in the 8-15 and 15-25 keV bands, similar to that observed with *HETE-2*/FREGATE. The hypothesis is marginally acceptable in the 25-50 keV and 350-1000 keV energy bands, and confidently accepted in the 50-100 and 100-350 keV bands. Noticing that BATSE is sensitive in 50-350 keV, we conclude that the BATSE observation is consistent with GBM observation in the 50-350 keV band, similar to that shown in Figure 4.

We compare the T_{90} in the 8-1000 keV band with that in the sub-energy bands in Figure 6. We still adopt $T_{90} = 2$ seconds in the 8-1000 keV band as the division line to classify LGRBs and SGRBs. One can find that some SGRBs in the 8-1000 keV band move to the LGRB group in softer bands. We investigate energy dependence of T_{90} for LGRBs only, since the SGRB sample is too small to give robust statistical result. The typical value of \bar{T}_{90} and its error $\Delta \log T_{90}$ for a given energy band are derived from a Gaussian fit to the $\log T_{90}$ distribution. Figure 7 shows \bar{T}_{90} as a function of the central value of the energy band. A clear correlation is found, and the best linear fit gives $\bar{T}_{90} \propto E^{-0.20 \pm 0.02}$. Note that the slopes are shallower than those observed in bright GRBs as reported by Richardson et al. (1996) and Bissaldi et al. (2011), who found $\bar{T}_{90} \propto E^{-0.4}$. This may be caused by a sample selection effect. A power-law index $\sim 0.2 \sim 0.3$ was also reported in the literature for energy dependence of GRB durations and pulse durations in some GRBs (e.g., Fenimore et al. 1995; Norris et al. 2005; Liang et al. 2006; Zhang 2008).

5. Extended Central Engine Activity Time in the X-ray and Optical Bands

As shown above, the burst duration is energy dependence and the bimodal T_{90} distribution would be due to instrumental selection effect. This suggests that if one goes to even lower energy bands, the duration can be even longer. Robotic optical telescopes also

detected significant optical flares in some GRBs. Li et al. (2012) presented a detail analysis on the optical flares. They got twenty-four optical flares from 19 GRBs and found that the isotropic flare peak luminosity ($L_{R,iso}$) is correlated with that of gamma-rays, i.e., $L_{R,iso} \propto L_{\gamma,iso}^{1.11 \pm 0.27}$. The flares peak at from tens of seconds to several days post the GRB trigger. Later flares tend to be wider and dimmer, following the relations $w \sim t_p/2$ and $L_{R,iso} \propto [t_p/(1+z)]^{-1.15 \pm 0.15}$. These results suggest that the optical flares are also related to the erratic behavior of the central engine.

The rapid slewing capacity of the X-ray telescope (XRT) onboard *Swift* makes it possible to catch the X-ray emission from very early to late episodes of GRBs. Erratic flares were detected for both LGRBs and SGRB (Burrows et al. 2005; Chincarini et al. 2007; Margutti et al. 2010). The detection probability of X-ray flares is much larger than that of optical flares (Li et al. 2012). It is generally believed that these X-ray flares are due to extended central engine activity at late times (Burrows et al. 2005; King et al. 2005; Fan & Wei 2005; Zhang et al. 2006; Dai et al. 2006; Perna et al. 2006; Proga & Zhang 2006; Liang et al. 2006; Lazzati & Perna 2007; Maxham & Zhang 2009). We take the peak time of the last X-ray flare to define the central engine duration of a burst (denoted as T_f). We make an extensive search for the significant flares in the *Swift*/XRT lightcurves with the following criteria. First, there are significant flares in the X-ray lightcurve, with $\Delta F/F \geq 5$, where $\Delta F = F_p - F$ is the flux over the underlying flux level F . Second, BAT and XRT lightcurves are well connected without a gap, or significant flares are observed after a gap. We show some examples of these lightcurves in Figure 8. We obtain a sample of 159 GRBs. Figure 9 shows T_f as a function of T_{90} . We find that there is no significant flare after T_{90} in 49 GRBs. This suggests that the T_{90} s of these bursts are comparable to the durations of the central engines. On the other hand, significant flares are observed in 110 GRBs after their T_{90} , indicating the T_f of these bursts are much larger than T_{90} . The X-ray emission of four GRBs, 050502B, 050724, 050904, and 060223, are dominated by flares (as shown in Figure 9), indicating that they may be super-LGRBs (Zou et al. 2006).

6. Conclusions and Discussion

We have calculated T_{90} of *Fermi*/GBM GRBs in various energy bands and compared the T_{90} distribution with those obtained from previous/current GRB survey missions. We show that the T_{90} distribution in the 8-1000 keV band is bimodal, being roughly consistent with that of the *CGRO*/BATSE GRB sample, but short-to-long GRB number ratio is 1:5, being lower than that in the BATSE sample (1:3). We measure the T_{90} in several sub-bands, i.e., 8-15, 15-25, 25-50, 50-100, 100-350, and 350-1000 keV bands to investigate the

energy band selection effect on the bimodal behavior of T_{90} distribution. It is found that the bimodal feature is well recognized in the 50-100 and 100-350 keV bands and only marginally accepted in the 25-50 keV and 350-1000 keV energy bands. The hypothesis of the bimodality is confidently rejected in 8-15 and 15-25 keV bands. We compare the T_{90} distributions in these sub-energy bands with those derived from other GRB detectors with similar energy bands and find that they are roughly consistent with each other. T_{90} as a function of energy band follows $\bar{T}_{90} \propto E^{-0.20 \pm 0.02}$ for LGRBs. Some GRBs fall into the short category in a high energy band, but move to the long category in a lower energy band. Considering the erratic optical and X-ray flares that may have the same physical origin as the prompt gamma-rays, the duration of a burst would be even much longer for most GRBs. These results indicate that T_{90} is energy dependent and the bimodal T_{90} distribution is valid only for certain energy bands.

Burst duration is critical for both GRB classification and understanding the behavior of GRB central engine. It is an indicator of the lifetime of GRB central engine. Popular central engine models of GRBs are related to accretion onto a central black hole that is formed from collapse of a massive star or merger of a compact star binary. Current favored jet launching models for GRBs include neutrino-annihilation mechanism from a neutrino-dominated accretion flow (NDAFs, e.g., Popham et al. 1999; Narayan et al. 2001; Kohri & Mineshige 2002; Di Matteo et al. 2002; Kohri et al. 2005; Gu et al. 2006; Chen & Beloborodov 2007; Liu et al. 2007; 2010; Xie et al. 2007; Lei et al. 2009) and Blandford-Znajek process (Blandford-Znajek 1977; Lee et al. 2000; Lei et al. 2007). It is theoretically expected that the accreting time scale for compact star mergers would be shorter than 1 s based on both analytical and numerical results (e.g., Narayan et al. 2001; Aloy et al. 2005). The T_{90} distribution observed with *CGRO*/BATSE (Kouveliotou et al. 1993) seems to be consistent with the speculation that two types of GRBs (long vs. short) are consistent with two distinct progenitors, i.e. collapses of massive stars vs. mergers of compact objects. However, as we have shown here, the bimodal T_{90} distribution would be likely due to an instrumental selection effect. Our results, together with the observed extended emission of some short GRBs, not only challenge the long-short GRB classification scheme, but also challenge the conventional GRB central engine models, and call for new mechanisms to account for extended GRB central engine activities (e.g., King et al. 2005; Fan & Wei 2005; Zhang et al. 2006; Dai et al. 2006; Perna et al. 2006; Proga & Zhang 2006; Metzger et al. 2008; Liu et al. 2012).

We acknowledge the use of the public data from the Swift data archive. We appreciate helpful comments from the referees. This work is supported by the “973” Program of China (2009CB824800), the National Natural Science Foundation of China (Grants No. 11025313,

11203008, 11078008, 11063001, and 11163001), the Special Foundation for Distinguished Expert Program of Guangxi, the Guangxi Natural Science Foundation (2010GXNSFA013112, 2011GXNSFB018063 and 2010GXNSFC013011), the special funding for national outstanding young scientist (Contract No. 2011-135), and the 3th Innovation Project of Guangxi University. BZ acknowledges support from NSF (AST-0908362).

REFERENCES

- Aloy, M. A., Janka, H.-T., Müller, E. 2005, *A&A*, 436, 273
- Ashman, K. M., Bird, C. M., & Zepf, S. E. 1994, *AJ*, 108, 2348
- Barthelmy, S. D., Chincarini, G., Burrows, D. N., et al. 2005, *Nature*, 438, 994
- Belczynski, K., Holz, D. E., Fryer, C. L., et al. 2010, *ApJ*, 708, 117
- Berger, E., Price, P. A., Cenko, S. B., et al. 2005, *Nature*, 438, 988
- Bissaldi, E., von Kienlin, A., Kouveliotou, C., et al. 2011, *ApJ*, 733, 97
- Blandford, R. D., & Znajek, R. L. 1977, *MNRAS*, 179, 433
- Bloom, J. S., Sigurdsson, S., & Pols, O. R. 1999, *MNRAS*, 305, 763
- Bloom, J., & Bay Area GRB Group 2006, *Bulletin of the American Astronomical Society*, 38, 379
- Burrows, D. et al. 2005, *Science*, 309, 1833
- Cobb, B. E., Bailyn, C. D., van Dokkum, P. G., & Natarajan, P. 2006, *ApJ*, 645, L113
- Colgate, S. A. 1974, *ApJ*, 187, 333
- Covino, S., Malesani, D., Israel, G. L., et al. 2006, *Gamma-Ray Bursts in the Swift Era*, 836, 54
- Chen, W.-X., & Beloborodov, A. M. 2007, *ApJ*, 657, 383
- Chincarini, G. et al. 2007, *ApJ*, 671, 1903
- Dai, Z. G., Wang, X. Y., Wu, X. F., & Zhang, B. 2006, *Science*, 311, 1127
- Di Matteo, T., Perna, R., & Narayan, R. 2002, *ApJ*, 579, 706

- Eichler, D., Livio, M., Piran, T., & Schramm, D. N. 1989, *Nature*, 340, 126
- Fan, Y. Z., & Wei, D. M. 2005, *MNRAS*, 364, L42
- Fan, Y.-Z., Zhang, B.-B., Xu, D., Liang, E.-W., & Zhang, B. 2011, *ApJ*, 726, 32
- Fenimore, E. E., in 't Zand, J. J. M., Norris, J. P., Bonnell, J. T., & Nemiroff, R. J. 1995, *ApJ*, 448, L101
- Fox, D. B., Frail, D. A., Price, P. A., et al. 2005, *Nature*, 437, 845
- Frontera, F., Guidorzi, C., Montanari, E., et al. 2009, *ApJS*, 180, 192
- Galama, T. J., Vreeswijk, P. M., van Paradijs, J., et al. 1998, *Nature*, 395, 670
- Gal-Yam, A., Fox, D. B., Price, P. A., et al. 2006, *Nature*, 444, 1053
- Gehrels, N. 2004, 5th INTEGRAL Workshop on the INTEGRAL Universe, 552, 777
- Gehrels, N., Sarazin, C. L., O'Brien, P. T., et al. 2005, *Nature*, 437, 851
- Gehrels, N., Norris, J. P., Barthelmy, S. D., et al. 2006, *Nature*, 444, 1044
- Goldstein, A., Preece, R. D., & Briggs, M. S. 2010, *ApJ*, 721, 1329
- Greiner, J., Krühler, T., Fynbo, J. P. U., et al. 2009, *ApJ*, 693, 1610
- Gu, W.-M., Liu, T., & Lu, J.-F. 2006, *ApJ*, 643, L87
- Hjorth, J., Sollerman, J., Møller, P., et al. 2003, *Nature*, 423, 847
- Hjorth, J., Watson, D., Fynbo, J. P. U., et al. 2005, *Nature*, 437, 859
- King, A., O'Brien, P. T., Goad, M. R., et al. 2005, *ApJ*, 630, L113
- Knigge, C., Coe, M. J., & Podsiadlowski, P. 2011, *Nature*, 479, 372
- Kohri, K., Narayan, R., & Piran, T. 2005, *ApJ*, 629, 341
- Kohri, K., & Mineshige, S. 2002, *ApJ*, 577, 311
- Kouveliotou, C., Meegan, C. A., Fishman, G. J., et al. 1993, *ApJ*, 413, L101
- Kulkarni, S. R., Frail, D. A., Wieringa, M. H., et al. 1998, *Nature*, 395, 663
- Lü, H.-J., Liang, E.-W., Zhang, B.-B., & Zhang, B. 2010, *ApJ*, 725, 1965

- Lamb, D. Q., Ricker, G. R., Atteia, J. -, et al. 2003, arXiv:astro-ph/0312503
- Lazzati, D. & Perna, R. 2007, MNRAS, 375, L46
- Lee, H. K., Wijers, R. A. M. J., & Brown, G. E. 2000, Phys. Rep., 325, 83
- Lei, W. H., Wang, D. X., Gong, B. P., & Huang, C. Y. 2007, A&A, 468, 563
- Lei, W. H., Wang, D. X., Zhang, L., et al. 2009, ApJ, 700, 1970
- Levesque, E. M., Bloom, J. S., Butler, N. R., et al. 2010, MNRAS, 401, 963
- Levesque, E. M., Soderberg, A. M., Foley, R. J., et al. 2010, ApJ, 709, L26
- Li, Liang, Liang, En-Wei, Tang, Qing-Wen, et al. 2012, ApJ, submitted (arXiv:1203.2332)
- Liang, E. W., Zhang, B., O'Brien, P. T., et al. 2006, ApJ, 646, 351
- Liang, E.-W., Zhang, B.-B., Stamatikos, M., et al. 2006, ApJ, 653, L81
- Lin, L., Liang, E.-W., Zhang, B.-B., & Zhang, S. N. 2008, American Institute of Physics Conference Series, 1065, 39
- Lin, L., Liang, E., & Zhang, S. 2010, Science in China G: Physics and Astronomy, 53, 64
- Liu, T., Liang, En-Wei, et al. 2012, ApJ, submitted
- Liu, T., Gu, W.-M., Xue, L., & Lu, J.-F. 2007, ApJ, 661, 1025
- Liu, T., Liang, E.-W., Gu, W.-M., et al. 2010, A&A, 516, A16
- Lu, R.-J., Wei, J.-J., Liang, E.-W., et al. 2012, ApJ, 756, 112
- Malesani, D., Tagliaferri, G., Chincarini, G., et al. 2004, ApJ, 609, L5
- Margutti, R. et al. 2010, MNRAS, 406, 2149
- Maxham, A. & Zhang, B. 2009, ApJ, 707, 1623
- McLachlan, G. J., & Basford, K. E. 1988, Statistics: Textbooks and Monographs, New York: Dekker, 1988,
- McLachlan, G. & Peel, D.A. 2000, in 'Finite Mixture Models', JOHN WILEY & SONS, INC. NewYork
- Metzger, B. D., Piro, A. L., & Quataert, E. 2008, MNRAS, 390, 781

- Mészáros, P. 2006, Reports on Progress in Physics, 69, 2259
- Mirabal, N., Halpern, J. P., An, D., Thorstensen, J. R., & Terndrup, D. M. 2006, ApJ, 643, L99
- Modjaz, M., Stanek, K. Z., Garnavich, P. M., et al. 2006, ApJ, 645, L21
- Nakar, E. 2007, Phys. Rep., 442, 166
- Narayan, R., Paczynski, B., & Piran, T. 1992, ApJ, 395, L83
- Narayan, R., Piran, T., & Kumar, P. 2001, ApJ, 557, 949
- Norris, J. P., Bonnell, J. T., Kazanas, D., et al. 2005, ApJ, 627, 324
- Norris, J. P., & Gehrels, N. 2008, American Institute of Physics Conference Series, 1000, 280
- Pélangéon, A., Atteia, J.-L., Nakagawa, Y. E., et al. 2008, A&A, 491, 157
- Paciesas, W. S., Meegan, C. A., Pendleton, G. N., et al. 1999, ApJS, 122, 465
- Paciesas, W. S., Meegan, C. A., von Kienlin, A., et al. 2012, arXiv:1201.3099
- Paczynski, B., & Sienkiewicz, R. 1981, ApJ, 248, L27
- Paczyński, B. 1991, American Institute of Physics Conference Series, 265, 144
- Perna, R., Armitage, P. J., & Zhang, B. 2006, ApJ, 636, L29
- Pian, E., Mazzali, P. A., Masetti, N., et al. 2006, Nature, 442, 1011
- Piran, T. 2005, Magnetic Fields in the Universe: From Laboratory and Stars to Primordial Structures., 784,164
- Popham, R., Woosley, S. E., & Fryer, C. 1999, ApJ, 518, 356
- Proga, D., & Zhang, B. 2006, MNRAS, 370, L61
- Qin, Y.-P., Xie, G.-Z., Xue, S.-J., et al. 2000, PASJ, 52, 759
- Richardson, G., Koshut, T., Paciesas, W., & Kouveliotou, C. 1996, American Institute of Physics Conference Series, 384, 87
- Sakamoto, T., Barthelmy, S. D., Baumgartner, W. H., et al. 2011, ApJS, 195, 2
- Salvatterra, R., Della Valle, M., Campana, S., et al. 2009, Nature, 461, 1258

- Savchenko, V., Neronov, A., & Courvoisier, T. J.-L. 2012, *A&A*, 541, A122
- Scargle, J. D. 1998, *ApJ*, 504, 405
- Schwarz, U. J. 1978, *A&A*, 65, 345
- Sollerman, J., Jaunsen, A. O., Fynbo, J. P. U., et al. 2006, *A&A*, 454, 503
- Stanek, K. Z., Bersier, D., Garnavich, P. M., Holland, S. T., & Matheson, T. 2003, *Bulletin of the American Astronomical Society*, 35, #132.03
- Starling, R. L. C., Wiersema, K., Levan, A. J., et al. 2011, *MNRAS*, 411, 2792
- Tanvir, N. R., Chapman, R., Levan, A. J., & Priddey, R. S. 2005, *Nature*, 438, 991
- Tanvir, N. R., Fox, D. B., Levan, A. J., et al. 2009, *Nature*, 461, 1254
- Virgili, F. J., Zhang, B., O’Brien, P., & Troja, E. 2011, *ApJ*, 727, 109
- Villasenor, J. S., Lamb, D. Q., Ricker, G. R., et al. 2005, *Nature*, 437, 855
- Woosley, S. E. 1993, *Bulletin of the American Astronomical Society*, 25, 894
- Woosley, S. E., & Bloom, J. S. 2006, *ARA&A*, 44, 507
- Xie, Y., Huang, C.-Y., & Lei, W.-H. 2007, *Chinese J. Astron. Astrophys.*, 7, 685
- Xin, L. P., Zheng, W. K., Wang, J., et al. 2010, *MNRAS*, 401, 2005
- Zhang, B. 2006, *Nature*, 444, 1010
- Zhang, B., & Mészáros, P. 2004, *International Journal of Modern Physics A*, 19, 2385
- Zhang, B., Zhang, B.-B., Liang, E.-W., et al. 2007, *ApJ*, 655, L25
- Zhang, B., Zhang, B.-B., Virgili, F. J., et al. 2009, *ApJ*, 703, 1696
- Zhang, F.-W. 2008, *ApJ*, 685, 1052
- Zhang, F.-W., Shao, L., Yan, J.-Z., & Wei, D.-M. 2012, *ApJ*, 750, 88
- Zou, Y. C., Dai, Z. G., & Xu, D. 2006, *ApJ*, 646, 1098

Table 1. Derived GBM T_{90} in different energy bands*

GBM ID	GRB name	8-15 keV (s)	15-25 keV (s)	25-50 keV (s)	50-100 keV (s)	100-350 keV (s)	350-1000 keV (s)	8-1000 keV (s)
080714745	080714	-	18.85±0.62	8.86±0.57	7.17±0.54	6.37±0.48	10.27±0.62	32.29±0.54
080725435	080725	21.79±0.58	25.12±0.44	31.58±0.4	22.27±0.46	22.88±0.54	3.36±0.66	22.21±0.23
080727964	080727C	-	25.7±0.66	29.12±0.66	32.77±0.66	27.36±0.69	-	35.55±0.59
080804972	080804	31.87±0.72	20.35±0.66	20.86±0.7	16.45±0.53	16.58±0.46	106.5±0.98	73.41±0.93
080810549	080810	50.91±0.99	51.39±0.76	52.7±0.83	25.92±0.69	39.39±0.88	125.28±1.12	49.34±0.63
080904886	080904	41.18±0.88	18.72±0.7	13.66±0.49	17.28±0.6	6.78±0.65	51.87±0.95	15.94±0.47
080905499	080905A	13.5±0.57	-	-	-	13.09±0.5	-	1.06±0.3
080905570	080905C	23.26±0.72	21.79±0.53	19.2±0.51	18.37±0.51	-	78.82±1	27.36±0.56
080905705	080905B	129.73±1.48	204.64±1.16	11.74±0.48	21.12±0.57	14.88±0.53	-	158.02±1.10
080906212	080906B	5.15±0.49	2.91±0.3	14.98±0.73	3.07±0.34	2.82±0.34	11.65±0.7	3.26±0.26
080912360	080912	57.63±0.83	35.78±0.75	16.67±0.72	17.44±0.62	-	92.29±1.16	17.89±0.49
080913735	080913B	32.64±0.78	37.73±0.5	25.18±0.62	14.5±0.67	14.82±0.76	149.54±1.48	25.31±0.52
080916009	080916C	58.24±0.85	68.54±0.95	63.52±1.04	61.47±0.62	56.96±0.58	36.77±0.74	63.65±0.61
080916406	080916A	40.35±0.7	44.58±0.7	32.03±0.6	140.22±1.14	20.99±0.57	214.88±1.39	44.26±0.72
080920268	080920	140.42±1.54	-	-	71.94±1.2	-	73.09±1.38	-
080925775	080925	19.81±0.62	16.51±0.47	25.5±0.76	15.58±0.44	14.72±0.4	0.96±0.64	23.33±0.62
080927480	080927	70.62±0.9	36.51±0.72	23.74±0.65	16.45±0.75	15.39±0.53	4.67±0.86	23.14±0.54
080928628	080928	33.86±0.51	18.5±0.49	21.44±0.69	14.05±0.66	47.2±0.99	84.48±0.91	24.54±0.44
081006604	081006	9.15±0.55	-	-	-	6.75±0.36	-	4.58±0.39
081006872	081006B	3.46±0.77	34.66±0.73	9.79±0.34	-	6.5±0.39	-	-
081008832	081008	111.94±1.39	198.66±1.2	20.7±0.52	19.68±0.68	20.7±0.62	215.3±1.54	175.2±1.16
081009140	081009	46.59±0.33	45.47±0.36	42.78±0.3	38.37±0.74	4.42±0.28	64.22±0.73	44.16±0.2
081012549	081012	25.02±0.59	-	-	12.86±0.6	14.66±0.55	93.44±1.22	14.08±0.42
081021398	081021	-	-	-	15.87±0.36	11.81±0.36	-	-
081024245	081024	-	-	-	2.94±0.34	-	-	0.13±0.18
081024891	081024B	-	-	107.23±1.05	1.25±1.08	50.72±0.94	86.4±0.9	-
081025349	081025	66.59±0.92	251.97±1.42	25.38±0.59	23.74±0.46	21.95±0.47	173.09±1.71	23.62±0.49
081028538	081028B	12.86±0.46	9.28±0.52	5.76±0.41	5.82±0.45	38.62±1.24	33.41±1.27	6.46±0.36
081101491	081101	-	2.37±0.33	-	-	0.35±0.26	4.96±0.36	0.54±0.39
081101532	081101B	12.42±0.55	8.86±0.49	8.51±0.46	7.71±0.3	7.78±0.2	-	8.1±0.25
081102365	081102B	38.94±0.96	-	-	30.59±0.66	50.34±0.9	-	2.34±0.43
081102739	081102	47.94±0.77	52.54±0.65	44.54±0.72	29.12±0.72	24.16±0.63	156.06±1.23	29.47±0.59
081105614	081105B	14.91±0.62	-	12.77±0.44	-	8.03±0.48	14.82±0.63	-
081107321	081107	3.42±0.25	1.98±0.28	7.01±0.58	2.37±0.29	1.57±0.25	-	1.73±0.14
081109293	081109A	-	-	31.46±0.54	24.96±0.66	39.87±0.77	50.11±0.85	27.46±0.65
081110601	081110	19.3±0.54	22.91±0.63	16.8±0.46	10.85±0.46	10.14±0.32	101.41±0.92	11.81±0.36
081113230	081113	4.45±0.27	-	0.83±0.32	-	0.45±0.23	-	0.74±0.25
081118876	081118	20.42±0.72	17.34±0.57	17.22±0.57	13.54±0.59	8±0.74	-	17.54±0.47
081119184	081119	4.16±0.4	3.87±0.32	-	0.93±0.3	-	-	-
081120618	081120	28.99±0.62	10.24±0.47	24.74±0.69	10.37±0.52	-	46.91±0.93	19.52±0.49
081121858	081121	23.46±0.52	18.21±0.48	18.18±0.46	19.74±0.49	17.09±0.57	37.82±0.73	55.20±0.84
081122520	081122	3.94±0.61	21.63±0.62	24.38±0.72	23.26±0.62	16.9±0.52	-	17.5±0.48
081122614	081122B	-	-	1.02±0.32	-	2.08±0.35	-	2.24±0.29
081124060	081124	22.78±0.75	19.97±0.51	18.88±0.47	14.27±0.51	15.78±0.52	-	22.82±0.58
081125496	081125	9.12±0.48	11.55±0.53	23.33±0.72	7.42±0.45	6.62±0.39	23.36±0.78	8.93±0.3
081126899	081126	39.1±0.98	36.26±0.69	36.54±0.73	38.5±0.66	36.54±0.75	8.32±1.23	35.36±0.46
081129161	081129	9.89±0.48	13.18±0.6	11.65±0.43	18.75±0.71	22.62±0.6	53.02±0.87	32±0.75
081130212	081130	-	-	44.35±0.69	-	-	-	-
081130629	081130B	4.16±0.41	5.18±0.41	6.53±0.36	7.81±0.36	4.45±0.39	-	13.5±0.59
081204004	081204C	10.21±0.49	2.85±0.48	15.42±0.47	2.14±0.39	2.75±0.45	-	2.94±0.32
081204517	081204B	-	0.83±0.28	0.35±0.16	0.58±0.23	0.45±0.23	0.8±0.34	0.48±0.16
081206275	081206	-	55.26±0.84	25.47±0.53	20.61±0.66	19.2±0.65	32.06±0.95	19.74±0.59
081206604	081206B	80.29±1.05	4.9±0.52	-	11.87±0.49	-	103.58±0.86	9.18±0.39
081206987	081206C	134.75±1.11	48.03±0.64	-	-	126.02±1.2	-	-
081207680	081207	127.58±1.27	90.11±0.77	92.42±0.85	104.99±1.02	88.48±1.02	64.26±0.99	99.39±0.85
081209981	081209	-	-	-	-	0.45±0.32	-	-
081213173	081213	1.73±0.37	-	-	-	-	3.14±0.29	-
081215784	081215	5.6±0.3	7.14±0.42	5.31±0.2	5.82±0.26	4.83±0.26	4.22±0.18	6.72±0.27
081215880	081215B	-	-	18.66±0.56	7.49±0.36	13.5±0.6	-	12.67±0.42
081216531	081216	6.05±0.32	1.41±0.41	1.15±0.23	0.77±0.23	0.38±0.14	3.2±0.45	0.9±0.14
081217983	081217	23.33±0.58	24.45±0.42	20.67±0.41	16.96±0.52	12.38±0.44	120.64±0.97	20.54±0.23
081221681	081221	32±0.97	30.75±0.72	29.15±0.63	28.86±0.62	12.1±0.57	-	45.82±0.99
081222204	081222	11.2±0.6	12.9±0.5	11.2±0.47	11.39±0.43	9.66±0.52	80.1±1.16	26.75±0.53
081223419	081223	-	1.09±0.23	2.27±0.26	0.38±0.14	0.45±0.14	0.96±0.37	0.61±0.16
081224887	081224	8.06±0.41	14.4±0.59	9.28±0.33	9.02±0.34	8.1±0.36	4.93±0.51	9.41±0.2
081226044	081226	-	7.84±0.39	-	1.73±0.54	22.62±0.6	-	0.48±0.2

Table 1—Continued

GBM ID	GRB name	8-15 keV (s)	15-25 keV (s)	25-50 keV (s)	50-100 keV (s)	100-350 keV (s)	350-1000 keV (s)	8-1000 keV (s)
081226156	081226C	16.51±0.69	15.04±0.62	12.61±0.51	13.76±0.66	59.42±0.78	44.83±1.16	13.79±0.6
081226509	081226B	—	—	—	—	0.77±0.36	10.02±0.53	0.51±0.32
081229187	081229	—	—	—	—	0.86±0.16	—	0.64±0.14
081231140	081231	26.91±0.59	27.17±0.52	39.14±0.63	25.7±0.34	25.63±0.36	—	26.56±0.23
090102122	090102	30.72±0.79	33.18±0.82	28.51±0.7	25.31±0.82	16.51±0.47	12.61±0.55	29.02±0.54
090107681	090107B	3.46±0.34	2.34±0.3	—	—	—	—	14.11±0.44
090108020	090108	1.15±0.5	1.25±0.48	6.14±0.56	0.77±0.36	0.96±0.45	30.62±1.07	1.02±0.36
090108322	090108B	—	—	—	—	0.8±0.54	—	0.67±0.39
090109332	090109	15.33±0.68	15.1±0.49	12.42±0.33	6.37±0.35	—	22.56±0.68	2.85±0.30
090112332	090112	27.23±0.72	13.7±0.65	9.15±0.6	7.87±0.45	7.55±0.56	—	7.9±0.34
090112729	090112B	15.52±0.64	13.38±0.57	9.92±0.52	8.93±0.48	7.58±0.39	—	12.61±0.49
090113778	090113	12.48±0.43	9.02±0.32	11.52±0.42	8.67±0.49	7.07±0.44	—	8.58±0.29
090117335	090117B	—	—	—	33.5±0.52	—	—	7.74±0.59
090117640	090117	8.96±0.46	15.07±0.5	6.08±0.57	18.85±0.58	—	6.05±0.36	16.03±0.59
090126227	090126B	7.49±0.54	10.66±0.44	16.1±0.68	9.25±0.57	—	—	8.26±0.54
090126245	090126C	—	—	—	21.44±0.7	—	23.14±0.82	—
090129880	090129	20.58±0.53	15.97±0.53	12.42±0.43	8.38±0.45	12.42±0.63	—	14.02±0.23
090131090	090131	35.36±0.5	34.24±0.53	33.47±0.49	32.06±0.43	34.75±0.75	58.91±0.76	36.06±0.48
090202347	090202	51.65±0.75	47.81±0.69	12.83±0.53	12.9±0.59	11.62±0.52	50.37±0.96	27.74±0.5
090206620	090206	25.22±0.66	30.05±0.66	—	0.67±0.4	35.65±0.72	—	0.74±0.3
090207777	090207	11.39±0.64	12.7±0.66	12.32±0.57	10.18±0.51	6.59±0.51	26.14±0.77	12.06±0.52
090217206	090217	32.38±0.82	33.54±0.65	32.42±0.56	29.76±0.65	25.82±0.68	7.87±0.55	30.59±0.53
090219074	090219	—	—	—	3.07±0.28	—	1.44±0.44	—
090222179	090222	30.18±0.84	73.73±0.95	19.14±0.65	18.62±0.55	11.84±0.5	32.96±0.93	15.62±0.42
090227772	090227B	0.58±0.28	7.07±0.36	4.06±0.39	0.38±0.23	0.96±0.29	2.94±0.43	0.96±0.23
090228976	090228B	40.06±0.75	5.63±0.54	48.48±0.74	36±0.69	3.1±0.52	42.78±0.86	6.08±0.41
090301315	090301B	—	93.28±0.92	31.87±0.59	5.73±0.61	6.82±0.48	—	5.98±0.52
090304216	090304	7.58±0.89	—	18.18±0.83	—	—	—	—
090305052	090305B	20.99±0.65	2.02±0.48	4.26±0.44	4.26±0.35	1.22±0.32	8.13±0.65	2.5±0.32
090306245	090306C	14.69±0.62	84.13±0.9	52.8±0.91	17.66±0.64	—	7.3±1.13	27.71±0.6
090308734	090308B	8±0.59	—	26.56±0.53	1.6±0.36	1.5±0.43	1.66±0.64	1.63±0.39
090310189	090310	184.86±1.33	14.11±1.06	30.75±0.53	48.51±0.67	3.01±0.51	—	122.11±0.85
090319622	090319	10.53±1.02	—	32.16±0.87	34.21±0.63	37.41±0.64	38.11±1.12	37.79±0.64
090320045	090320C	64.54±0.98	—	3.65±0.59	—	—	22.72±0.56	6.43±0.26
090320418	090320A	4.38±0.48	21.38±0.47	8.7±0.45	3.1±0.26	3.71±0.23	5.76±0.73	6.46±0.29
090320801	090320B	15.46±0.54	52.96±0.64	29.57±0.62	39.23±0.67	6.21±0.55	111.81±1.26	29.89±0.55
090323002	090323	78.3±1.06	61.38±0.79	60.77±0.64	61.25±0.65	59.58±0.56	12.29±1	60.51±0.53
090326633	090326	8.26±0.46	10.56±0.55	10.37±0.52	11.39±0.51	46.82±0.8	—	10.37±0.51
090327404	090327	29.92±0.77	15.01±0.58	18.11±0.53	13.41±0.68	12.48±0.6	45.47±0.72	16.42±0.57
090328713	90328B	—	—	2.91±0.34	0.26±0.19	0.48±0.25	1.89±0.39	0.29±0.19
090330279	090330	132.74±1.26	214.69±1.19	256.45±1.54	33.34±0.59	74.62±1.81	125.5±1.82	24.90±0.51
090331681	090331	179.36±1.27	138.34±1.16	207.42±1.47	214.46±1.52	—	179.81±1.7	0.38±0.37
090403314	090403	27.33±0.66	—	—	—	8.13±0.5	—	14.3±0.58
090405663	090405	—	2.08±0.3	0.67±0.3	—	—	—	0.64±0.33
090409288	090409	—	—	—	22.4±0.51	13.57±0.6	—	49.79±0.65
090411838	090411	18.18±0.56	15.42±0.57	15.65±0.54	18.85±0.74	16.29±0.6	—	15.81±0.47
090411991	090411B	36.54±0.89	16.99±0.56	15.3±0.54	14.02±0.69	14.94±0.54	—	17.34±0.43
090412061	090412	—	—	—	—	5.76±0.43	2.11±0.2	1.47±0.41
090418816	090418C	—	0.42±0.16	—	—	—	—	—
090422150	090422	—	—	13.34±0.54	1.38±0.52	17.73±0.52	—	—
090423330	090423	—	12.67±0.59	36.67±0.72	52.83±0.84	—	—	12.35±0.5
090424592	090424	57.38±0.8	46.21±0.64	34.46±0.8	4.83±0.23	24.7±0.96	3.94±0.52	16.52±0.32
090425377	090425	18.18±0.85	18.27±0.83	67.49±0.76	75.58±0.79	12.38±0.81	40.96±1.29	73.41±0.61
090426066	090426B	12.77±0.4	9.12±0.46	—	—	—	3.65±0.59	12.83±0.39
090426690	090426C	5.22±0.43	6.53±0.45	3.78±0.5	3.42±0.48	4.8±0.5	—	5.06±0.41
090427644	090427B	—	—	—	—	—	20.45±0.76	1.57±0.40
090427688	090427C	—	11.2±0.56	12.26±0.54	15.14±0.64	—	—	12.48±0.53
090428552	090428B	18.91±0.59	19.62±0.71	12.19±0.44	11.01±0.5	15.01±0.57	50.98±1.05	29.02±0.59
090429530	090429C	18.02±0.48	14.14±0.46	—	10.34±0.44	9.98±0.56	13.54±0.53	10.24±0.36
090429753	090429D	—	—	2.4±0.48	0.61±0.34	7.68±0.51	53.34±1.04	1.98±0.45
090502777	090502	56.1±0.85	22.21±0.83	31.49±0.92	54.66±0.66	—	32.77±1.1	59.78±0.73
090509215	090509	141.28±1.69	36.61±0.57	247.14±1.23	31.97±0.74	26.21±0.64	120.93±1.97	261.18±1.08
090510016	090510	0.48±0.25	0.38±0.14	0.64±0.19	0.42±0.12	0.35±0.07	0.38±0.14	0.38±0.05
090510325	090510B	—	29.12±0.63	28.29±0.61	18.53±0.36	7.2±0.39	—	10.59±0.46
090511684	090511	—	36.83±0.63	4.48±0.45	1.66±0.45	9.95±0.52	—	5.22±0.43
090513916	090513	28.93±0.79	—	—	24.16±0.68	18.66±0.68	—	18.46±0.52

Table 1—Continued

GBM ID	GRB name	8-15 keV (s)	15-25 keV (s)	25-50 keV (s)	50-100 keV (s)	100-350 keV (s)	350-1000 keV (s)	8-1000 keV (s)
090513941	090513B	—	—	46.11±0.72	17.41±0.59	13.95±0.5	44.42±0.75	12.74±0.46
090514006	090514	43.97±0.73	42.78±0.66	50.37±0.71	43.1±0.62	31.23±0.57	—	45.28±0.54
090516137	090516B	—	97.02±1.22	—	—	—	—	126.27±1.59
090516353	090516	95.62±1.02	93.5±0.81	89.34±0.66	84.58±0.86	102.69±1	—	93.38±0.49
090516853	090516C	16.13±0.63	17.95±0.68	13.28±0.44	11.17±0.59	10.78±0.6	24.67±0.79	13.98±0.39
090518080	090518	50.72±2.29	75.42±0.99	20.13±0.37	38.66±0.73	8.32±0.5	55.58±0.84	7.97±0.44
090518244	090518B	10.88±0.73	9.15±0.6	8.03±0.57	6.75±0.52	5.98±0.49	—	6.62±0.4
090519462	090519B	139.52±1.3	—	—	—	12.1±0.46	—	37.79±0.50
090519881	090519	45.86±1.56	87.97±1.53	—	14.98±0.56	252.58±1.53	—	42.88±0.57
090520832	090520B	20.61±0.68	—	—	—	—	54.08±1.25	—
090520850	090520C	8.48±0.43	7.01±0.4	4.22±0.33	3.81±0.25	4.1±0.37	4.16±0.64	4.03±0.23
090520876	090520D	17.15±0.72	14.62±0.64	15.58±0.56	11.65±0.43	18.98±0.72	43.65±0.73	14.37±0.5
090522344	090522	—	28.06±0.62	11.97±0.54	8.16±0.53	—	44.99±1.12	19.26±0.57
090524346	090524	46.88±0.7	52.29±0.72	50.21±0.66	48.42±0.68	46.46±0.57	67.01±1.37	50.46±0.58
090528173	090528	33.95±0.8	32.13±0.66	33.18±0.62	27.46±0.63	25.82±0.69	—	29.06±0.55
090528516	090528B	106.21±0.92	100.54±0.89	91.52±0.87	76.48±0.93	44.38±0.69	—	92.1±0.73
090529310	090529B	25.09±0.57	4.8±0.54	21.79±0.59	4.83±0.48	45.31±0.89	5.92±0.84	4.29±0.45
090529564	090529C	12.9±0.69	10.21±0.39	10.4±0.34	9.86±0.23	9.63±0.25	38.98±0.82	10.14±0.25
090530760	090530B	147.42±1.33	143.97±1.09	131.36±1.27	114.34±1.14	89.76±1.07	175.68±1.72	135.68±0.91
090531775	90531B	—	—	23.84±0.56	2.5±0.54	2.02±0.48	14.94±0.58	2.02±0.39
090602564	090602	47.36±0.75	—	—	10.53±0.52	13.79±0.61	44.22±0.61	13.66±0.49
090606471	090606	—	96.64±1.03	—	37.57±0.98	41.44±1.39	64.26±1.25	—
090608052	090608	24.32±1	9.82±0.58	10.14±0.48	30.37±0.6	22.11±0.46	—	8.22±0.35
090610723	090610B	179.74±1.19	196.93±1.54	100.61±1.39	142.43±1.23	122.24±1.59	46.05±1.61	140.74±0.83
090610883	090610C	13.15±0.42	13.18±0.39	13.15±0.42	13.15±0.42	13.15±0.42	13.18±0.39	13.15±0.42
090612619	090612	34.3±0.59	4.19±0.57	5.18±0.5	4.99±0.42	5.79±0.58	30.88±0.9	7.23±0.55
090616157	090616	—	—	26.43±0.76	5.76±0.73	—	—	2.08±0.61
090617208	090617	2.14±0.34	—	—	0.99±0.25	0.22±0.07	1.47±0.29	0.26±0.14
090618353	090618	169.25±1.43	118.88±1.15	130.53±1.3	107.58±1.06	104.83±0.93	25.47±0.99	130.24±1.05
090620400	090620	18.98±0.79	10.75±0.6	13.95±0.55	10.91±0.52	7.3±0.37	41.98±0.96	14.34±0.47
090621185	090621	50.62±0.87	61.86±1.02	67.33±1.03	44.16±0.89	51.87±0.92	85.47±1.13	63.71±0.9
090621417	090621C	47.04±0.69	41.66±0.73	35.17±0.69	30.75±0.64	23.23±0.63	—	36.42±0.57
090621447	090621D	38.11±0.58	23.23±0.72	28.99±0.6	20.1±0.56	21.06±0.6	181.44±1.68	21.63±0.53
090621922	090621B	—	3.33±0.28	—	0.29±0.16	0.19±0.1	—	0.29±0.16
090623107	090623	79.9±1	41.44±0.73	44.29±0.76	52.1±0.73	87.46±1.01	129.06±1.15	62.59±0.75
090625234	090625	—	—	23.2±0.49	13.86±0.48	10.08±0.48	187.26±1.68	16.26±0.46
090625560	090625B	40.26±0.96	88.99±0.92	23.36±0.92	18.43±0.6	19.94±0.59	—	6.85±0.45
090626189	090626	53.5±0.72	48±0.59	45.31±0.33	45.18±0.33	44.54±0.45	2.66±0.39	47.07±0.55
090630311	090630	22.98±0.37	11.55±0.67	3.46±0.45	2.94±0.55	23.52±0.5	31.52±0.85	10.08±0.52
090701225	090701	—	12.48±0.73	—	19.33±0.64	—	37.41±0.66	—
090703329	090703	28.8±0.69	15.68±0.6	22.72±0.49	6.56±0.48	40.99±0.7	2.08±0.84	9.15±0.55
090704242	090704	54.43±1.05	60.99±0.8	58.82±0.85	59.71±0.67	48.54±0.72	—	58.69±0.62
090706283	090706	—	—	—	18.69±0.37	—	—	—
090708152	090708	15.52±0.49	42.82±0.85	7.84±0.48	34.69±0.61	31.84±0.69	—	12.48±0.39
090709630	090709B	79.36±0.95	4.06±0.39	11.97±0.47	9.7±0.39	12.19±0.49	96.8±1.11	11.14±0.32
090712160	090712	—	—	53.47±0.8	51.78±0.79	31.94±0.55	55.36±0.87	31.68±0.62
090713020	090713	—	50.02±0.8	47.87±0.8	43.2±0.79	153.63±1.35	131.9±1.35	49.86±0.73
090717034	090717	—	—	—	10.46±0.53	55.65±0.94	76.58±1.25	65.63±0.93
090717111	090717B	—	—	—	0.67±0.25	0.58±0.23	1.44±0.39	—
090718720	090718	90.21±1.22	15.1±1.04	—	—	—	—	—
090718762	090718B	22.02±0.73	24.74±0.86	20.16±0.68	21.47±0.67	17.92±0.55	—	21.41±0.48
090719063	090719	33.28±0.57	12.06±0.76	12.74±0.6	10.85±0.48	9.02±0.47	11.71±0.75	11.49±0.4
090720276	090720	5.34±0.52	5.5±0.51	5.89±0.51	3.23±0.39	5.09±0.57	—	5.6±0.4
090720710	090720B	—	—	6.46±0.54	8.06±0.49	7.33±0.39	9.25±0.54	8.64±0.51
090802235	090802	—	—	—	—	0.19±0.5	2.4±0.58	—
090802666	090802B	—	19.78±0.7	19.46±0.51	13.89±0.57	55.68±0.89	—	18.21±0.53
090807832	090807B	5.63±0.59	6.34±0.5	1.73±0.42	1.25±0.57	—	—	45.79±1.34
090809978	090809B	13.34±0.7	12.7±0.52	10.08±0.49	9.5±0.52	12.9±0.66	2.85±0.58	13.22±0.52
090813174	090813	10.27±0.66	9.12±0.61	13.66±0.61	2.5±0.51	10.82±0.7	47.42±0.93	8.96±0.55
090814368	090814C	—	—	—	1.31±0.25	0.26±0.14	—	0.51±0.18
090815438	090815B	23.04±0.65	26.5±0.6	24.26±0.65	23.65±0.66	12.16±0.72	82.91±1.41	25.28±0.52
090817036	090817	75.9±0.88	89.44±1.92	33.25±0.73	10.37±0.52	12.99±0.53	259.87±1.65	33.47±0.59
090820027	090820	6.18±0.3	5.76±0.18	4.86±0.09	6.18±0.12	6.08±0.09	6.62±0.66	6.24±0.07
090820509	090820B	20.38±0.58	11.23±0.59	12.06±0.61	1.86±0.59	11.97±0.82	40.9±0.89	11.87±0.49
090826068	090826	28.8±0.66	25.44±0.69	—	16.83±0.72	20.13±0.56	—	10.02±0.43
090828099	090828	23.42±1.09	23.78±0.84	19.23±0.76	19.58±0.87	16.48±0.77	120.32±1.32	88.96±0.97

Table 1—Continued

GBM ID	GRB name	8-15 keV (s)	15-25 keV (s)	25-50 keV (s)	50-100 keV (s)	100-350 keV (s)	350-1000 keV (s)	8-1000 keV (s)
090829672	090829	73.22±1.15	70.85±0.93	74.72±0.78	62.66±1.03	49.02±1	145.79±1.22	77.79±0.78
090829702	090829B	55.36±0.81	26.69±0.57	18.21±0.49	18.37±0.47	92.8±0.92	—	129.02±0.92
090831317	090831	59.84±0.96	54.14±0.94	40.86±0.7	157.18±1.23	41.18±0.62	152.83±1.68	58.34±0.68
090902401	090902	11.3±0.63	—	11.01±0.51	1.15±0.27	2.62±0.34	10.75±0.55	1.28±0.28
090904058	090904B	50.53±0.89	51.87±0.79	53.15±0.72	52.16±0.75	53.34±0.77	82.21±1.2	52.35±0.59
090910812	090910	38.53±0.69	40.38±0.52	40.1±0.44	121.31±1.02	38.91±0.73	—	40.19±0.23
090912660	090912	262.5±1.53	55.94±1.06	169.15±0.87	120.03±0.9	9.06±0.39	—	126.37±0.54
090922539	090922A	96.58±1.09	88.48±0.9	87.17±0.83	88.03±0.95	7.17±0.46	100.7±1.02	88.42±0.68
090926181	090926	13.92±0.42	19.84±0.74	13.5±0.2	12.29±0.45	11.39±0.2	10.34±0.62	17.63±0.55
090926914	090926B	31.1±0.74	32.13±0.79	35.26±0.75	41.82±0.72	35.17±0.7	29.89±1.27	41.34±0.62
090927422	090927	2.27±0.48	—	—	1.25±0.44	—	—	3.2±0.32
090929190	090929A	53.38±1.08	8.74±0.52	4.8±0.36	5.89±0.4	4.29±0.29	2.21±0.48	7.81±0.45
091003191	091003	21.22±0.58	20.03±0.51	21.34±0.52	20.58±0.39	20.67±0.39	18.78±0.66	23.17±0.57
091010113	091010	8.64±0.49	7.65±0.32	6.94±0.27	6.18±0.27	5.89±0.33	—	7.58±0.3
091020900	091020	11.84±0.54	47.42±0.87	12.67±0.52	16.83±0.7	30.5±0.78	—	44.67±0.65
091024372	091024	70.53±0.87	22.53±0.57	66.02±0.82	49.63±0.84	44.1±0.59	—	48.26±0.62
091026550	091026	14.14±0.55	—	—	24.99±0.74	6.88±0.43	28.77±0.91	15.74±0.46
091030828	091030	26.08±0.84	143.17±1.32	36.54±0.59	99.55±0.91	35.65±0.57	19.52±0.83	97.63±0.81
091031500	091031	11.49±0.57	37.41±0.59	16.35±0.64	16.13±0.51	15.97±0.43	20.83±0.73	37.86±0.66
091102607	091102	—	7.2±0.57	6.78±0.5	7.49±0.56	6.53±0.5	—	7.58±0.46
091112737	091112	68.03±0.95	36.74±0.72	19.49±0.68	15.39±0.63	15.49±0.51	58.5±0.97	50.85±0.82
091120191	091120	54.46±0.82	50.91±0.64	50.72±0.58	51.39±0.53	51.62±0.66	—	50.94±0.43
091123298	091123	55.71±1.75	203.04±1.41	184.13±1.09	174.98±1.09	177.95±1.13	86.05±2.07	200.61±1.14
091126333	091126	—	—	1.06±0.34	0.29±0.16	0.29±0.17	1.6±0.42	0.32±0.18
091126389	091126B	—	—	—	—	—	—	0.86±0.3
091127976	091127	10.24±0.43	9.63±0.42	8.45±0.33	7.71±0.3	5.92±0.5	20.99±0.74	9.15±0.26
091128285	091128	72.67±1.02	51.9±0.73	38.18±0.62	39.07±0.66	30.05±0.7	—	37.82±0.53
091208410	091208B	10.27±0.32	11.81±0.26	11.9±0.24	12.7±0.36	2.62±0.36	—	11.39±0.14
091221870	091221	68.93±0.9	24.32±0.77	80.58±1.02	30.78±0.66	16.03±0.52	—	30.43±0.62
100111176	100111A	—	46.66±0.81	41.63±0.76	12.54±0.65	—	47.49±0.79	11.01±0.46
100116897	100116A	19.17±1.15	15.97±0.97	100.06±0.9	16.83±0.95	102.21±0.87	7.78±1.06	100.93±0.71
100117879	100117A	—	—	—	0.48±0.21	0.51±0.32	2.34±0.26	0.51±0.19
100122616	100122A	8.13±0.43	9.15±0.45	7.65±0.36	6.3±0.37	5.34±0.4	—	7.94±0.33
100130729	100130A	36.26±1.07	106.4±0.98	96.67±0.82	93.5±0.82	23.55±1.06	—	93.92±0.68
100130777	100130B	58.66±0.9	41.47±0.74	69.41±0.95	44.32±0.63	42.62±0.82	137.18±1.16	71.07±0.76
100131730	100131A	3.62±0.39	3.68±0.3	3.49±0.2	3.26±0.19	3.14±0.28	2.4±0.48	3.14±0.14
100205490	100205B	31.68±0.61	21.18±0.68	36.9±0.72	8.67±0.53	15.52±0.73	—	14.3±0.44
100206563	100206A	—	1.76±0.39	0.48±0.26	1.18±0.12	0.22±0.16	—	0.19±0.13
100212588	100212A	5.82±0.41	11.33±0.46	17.44±0.48	—	—	9.18±0.49	8.1±0.46
100218194	100218A	14.53±1	—	57.28±0.83	30.27±0.72	36.1±0.63	—	31.33±0.7
100223110	100223A	—	—	—	0.51±0.19	0.26±0.09	0.22±0.16	0.26±0.1
100224112	100224B	33.34±0.61	87.3±0.93	77.98±0.82	74.18±0.91	113.38±1.13	27.01±1.16	76.42±0.81
100225115	100225A	68.77±0.99	34.91±0.73	11.26±0.45	19.74±0.57	13.34±0.58	20.48±0.56	13.02±0.44
100322045	100322A	38.21±0.79	36.29±0.45	36.64±0.36	36.48±0.33	36.93±0.28	10.43±0.77	36.83±0.21
100325275	100325A	9.06±0.39	7.81±0.41	15.62±0.57	6.98±0.32	6.78±0.32	2.78±0.52	7.52±0.25
100401297	100401A	181.73±2.18	127.68±1.17	—	91.87±1.5	—	—	89.06±1.32
100413732	100413A	204.99±1.57	173.95±1.46	213.57±1.17	170.46±1.23	62.3±1.25	192.74±2.09	120.06±1.00
100414097	100414A	23.52±0.66	24.45±0.6	47.3±0.79	44.03±1.09	22.05±0.3	21.31±0.54	22.53±0.32
100423244	100423B	47.9±0.64	63.23±0.79	21.98±0.66	21.09±0.67	11.97±0.55	23.46±0.84	19.84±0.55
100427356	100427A	26.08±0.68	7.14±0.52	9.38±0.58	9.79±0.56	10.56±0.55	—	10.43±0.41
100503554	100503A	102.85±0.96	20.45±0.89	149.47±1.31	135.97±1.2	24.64±0.8	—	147.58±1.09
100504806	100504A	52.67±0.92	22.75±0.59	19.55±0.73	22.82±0.68	12.93±0.6	—	24.51±0.73
100510810	100510A	45.44±0.83	18.14±0.58	21.06±0.56	16.74±0.54	18.78±0.68	65.86±0.83	19.81±0.54
100511035	100511A	31.94±0.7	33.34±0.61	44.7±0.78	43.04±0.66	29.63±0.78	15.3±0.69	41.41±0.67
100522157	100522A	36.42±0.67	36.58±0.62	37.28±0.56	3.26±0.32	3.1±0.34	—	37.38±0.59
100528075	100528A	16.99±0.53	24.93±0.62	19.01±0.66	15.58±0.6	14.72±0.59	18.59±0.95	22.98±0.67
100615083	100615A	34.18±0.75	36±0.72	39.3±0.99	37.47±0.84	34.05±0.75	65.31±1.13	36.42±0.59
100619015	100619A	96.22±0.92	12.83±1.02	95.04±0.73	92.61±0.71	92.22±0.85	—	92.61±0.34
100625773	100625A	—	0.64±0.3	—	1.63±0.36	0.26±0.05	—	0.38±0.14
100701490	100701B	52.22±0.69	11.36±0.57	7.58±0.52	15.33±0.64	22.59±0.81	8.1±0.49	25.02±0.63
100704149	100704A	141.06±1.82	262.11±1.55	14.56±0.59	12.19±0.6	11.14±0.56	152.13±1.64	183.62±1.12
100707032	100707A	70.75±0.81	—	17.98±0.43	14.62±0.4	11.9±0.33	6.75±0.56	15.55±0.43
100722096	100722A	7.74±0.46	8.16±0.46	7.3±0.34	9.22±0.73	3.81±0.46	—	7.36±0.28
100724029	100724B	118.14±1.03	119.04±0.69	118.53±0.75	116±0.95	104.54±1.14	68.8±0.69	116.51±0.56
100727238	100727A	23.17±0.53	26.91±0.54	22.18±0.48	42.46±0.76	—	—	25.92±0.47
100728095	100728A	118.46±1.06	147.1±1.06	157.95±1	157.82±1.08	158.34±1.52	45.09±1.04	159.97±0.76

Table 1—Continued

GBM ID	GRB name	8-15 keV (s)	15-25 keV (s)	25-50 keV (s)	50-100 keV (s)	100-350 keV (s)	350-1000 keV (s)	8-1000 keV (s)
100728439	100728B	5.28±0.52	12.54±0.55	9.66±0.51	8.67±0.52	9.15±0.55	—	9.34±0.46
100802240	100802A	134.3±0.94	273.12±1.59	182.4±1.24	131.71±1.12	10.14±0.43	180.48±1.2	132.26±0.84
100814160	100814A	154.21±0.92	76.83±0.7	138.21±0.92	133.41±0.92	16.32±0.52	173.98±1.87	25.41±0.29
100814351	100814B	8.74±0.44	5.06±0.27	4.19±0.34	6.34±0.37	5.98±0.34	—	5.18±0.32
100816026	100816A	2.53±0.39	2.14±0.3	2.5±0.34	2.3±0.28	2.18±0.36	—	2.24±0.23
100906576	100906A	118.11±0.9	119.33±1	109.92±0.87	16.1±0.56	11.84±0.29	100.45±1.3	115.55±0.68
100910818	100910A	13.44±0.47	13.28±0.32	13.06±0.23	12.1±0.28	8.64±0.24	—	13.38±0.29
100915243	100915B	—	58.85±0.72	51.68±0.86	12.42±0.45	8.8±0.39	—	5.76±0.45
100924165	100924A	11.17±0.44	13.02±0.49	15.78±0.66	7.04±0.32	2.91±0.39	—	11.87±0.44
101008697	101008A	—	18.53±0.53	22.66±0.71	14.37±0.54	14.02±0.52	—	7.2±0.3
101011707	101011A	—	109.18±1.05	—	102.37±1.1	34.62±0.62	—	38.5±0.62
101014175	101014A	207.81±0.47	208.54±0.37	210.75±0.39	214.14±0.58	219.23±1.02	249.63±1.77	211.17±0.16
101023951	101023A	24.42±0.84	72.8±0.83	75.78±0.81	75.42±0.88	71.1±0.94	10.69±1.18	66.94±0.55
101024486	101024A	—	1.06±0.57	—	1.47±0.46	11.49±0.57	—	20.51±0.54
101112924	101112A	3.84±0.45	6.88±0.43	15.3±0.4	3.94±0.49	6.18±0.48	29.89±0.8	3.97±0.32
101123952	101123A	102.56±0.8	103.07±0.7	103.94±0.67	102.37±0.56	101.41±0.6	17.25±0.92	103.01±0.44
101129652	101129A	—	—	—	0.67±0.25	0.54±0.23	—	0.54±0.17
101201418	101201A	68±0.87	63.87±0.76	64.64±0.77	56.96±0.79	62.05±1	33.73±1.23	83.62±0.68
101213451	101213A	51.71±0.76	50.56±0.77	28.29±0.6	23.84±0.48	24.7±0.43	81.47±0.96	38.24±0.56
101219686	101219B	—	—	32.1±0.54	58.05±0.83	20.64±0.49	—	54.21±0.75
101224227	101224A	—	—	0.61±0.3	0.45±0.19	—	—	0.58±0.32
110102788	110102A	128.99±0.74	137.5±0.68	136.77±0.75	132.93±0.81	132.45±0.74	—	133.76±0.34
110106893	110106B	24.54±0.76	29.79±0.63	27.36±0.63	24.64±0.7	34.62±0.67	—	22.78±0.62
110112934	110112B	—	1.66±0.3	—	—	0.35±0.2	—	0.26±0.09
110119931	110119A	258.37±1.47	28.16±0.91	67.33±0.63	58.82±0.76	60.93±0.81	280.74±1.88	59.87±0.59
110120666	110120A	—	3.84±0.54	9.82±0.52	22.4±0.59	13.06±0.43	22.53±0.67	16.06±0.39
110123804	110123A	16.45±0.55	20.22±0.63	19.1±0.5	17.15±0.52	15.94±0.46	46.94±0.63	17.18±0.42
110125894	110125A	4.77±0.39	3.81±0.39	2.5±0.45	5.02±0.39	6.5±0.44	—	4.1±0.32
110128073	110128A	69.5±1.12	—	12.77±0.79	—	70.5±0.74	67.78±0.85	—
110201399	110201A	—	—	42.78±0.6	13.41±0.53	4.29±0.36	—	11.71±0.51
110207470	110207A	12.06±0.84	18.4±0.66	47.26±0.8	38.08±0.73	0.51±0.29	43.71±0.87	39.01±0.52
110213220	110213A	35.81±0.63	33.06±0.64	30.98±0.57	32.58±0.67	14.56±0.67	29.54±1.11	33.12±0.46
110301214	110301A	7.55±0.33	7.14±0.3	5.95±0.2	5.38±0.23	5.06±0.16	9.76±0.6	6.14±0.13
110318552	110318A	13.79±0.76	15.68±0.5	9.95±0.54	11.62±0.75	5.22±0.48	46.4±0.82	14.66±0.41
110319815	110319B	—	—	49.12±0.8	—	53.5±0.69	—	13.95±0.52
110328520	110328B	49.7±0.79	82.75±0.87	44.03±0.77	77.6±0.9	93.89±1.13	29.89±0.72	71.55±0.82
110401920	110401A	4.51±0.53	20.83±0.5	3.39±0.32	1.06±0.25	0.96±0.23	—	2.82±0.28
110402009	110402A	—	68.19±0.66	72.38±0.76	33.18±0.68	33.79±0.75	—	35.17±0.53
110412315	110412A	21.31±0.7	25.73±0.65	18.11±0.55	15.74±0.6	10.53±0.52	—	17.38±0.53
110420946	110420B	—	—	0.7±0.28	0.35±0.17	—	—	0.74±0.25
110529034	110529A	0.93±0.3	0.83±0.33	8.19±0.3	1.12±0.25	0.58±0.24	0.19±0.2	0.64±0.19
110610640	110610A	48.35±0.92	45.02±0.63	49.25±0.58	42.34±0.68	40.35±0.7	—	39.94±0.55
110625881	110625A	37.98±0.8	49.31±0.8	36.13±0.92	27.33±0.63	25.18±0.26	42.21±0.87	30.75±0.71
110705151	110705A	—	0.7±0.23	0.35±0.17	0.29±0.13	0.35±0.07	0.19±0.1	0.35±0.07
110709642	110709A	44.74±0.7	43.26±0.76	42.66±0.64	39.58±0.7	36.06±0.52	54.78±0.89	42.11±0.67
110721200	110721A	10.88±0.47	12.64±0.56	57.82±0.81	16.61±0.62	15.62±0.64	11.23±0.74	17.73±0.45
110731465	110731A	8.9±0.47	8.03±0.46	8.26±0.4	6.94±0.2	6.56±0.16	8.77±0.59	6.98±0.14
110818860	110818A	73.6±1.07	73.44±0.96	222.88±1.48	53.95±0.83	55.84±0.94	89.12±1.34	62.88±0.82
110825102	110825A	69.86±0.82	68.61±0.75	64.42±0.54	7.26±0.16	6.56±0.2	5.66±0.57	67.2±0.61
110903111	110903A	233.34±1.75	239.52±1.35	228.19±1.19	215.46±1.08	220.1±1.16	249.63±1.59	227.81±1.02
110921577	110921A	107.14±0.92	23.2±0.52	23.97±0.54	15.55±0.62	17.76±0.52	84.61±0.93	15.01±0.44

Available in the electronic version only.

Table 2: The ratio of short to long GRB numbers with a division of $T_{90} = 2$ seconds for samples observed with different GRB missions and for *Fermi*/GBM observations in some bands. The results of bimodal distribution test with the KMM algorithm are also reported.

Instrument	Band (keV)	SGRB:LGRB	p_{KMM}
<i>HETE-2</i> /FREGATE	6-80	0:82	0.32
<i>SWIFT</i> /BAT	15-150	51:557	7.5×10^{-22}
<i>BeppoSAX</i> /GRBM	40-700	111:892	1.8×10^{-18}
<i>Fermi</i> /GBM	8-1000	39:253	1.0×10^{-11}
<i>CGRO</i> /BATSE	50-300	500:1541	0
<i>INTEGRAL</i> /SPI-ACS	20-8000	196:724	3.0×10^{-30}
GBM-1	8-15	5:236	2.25×10^{-2}
GBM-2	15-25	13:237	5.9×10^{-4}
GBM-3	25-50	12:246	1.1×10^{-5}
GBM-4	50-100	35:248	6.6×10^{-8}
GBM-5	100-350	32:240	3.4×10^{-11}
GBM-6	350-1000	13:177	1.2×10^{-5}

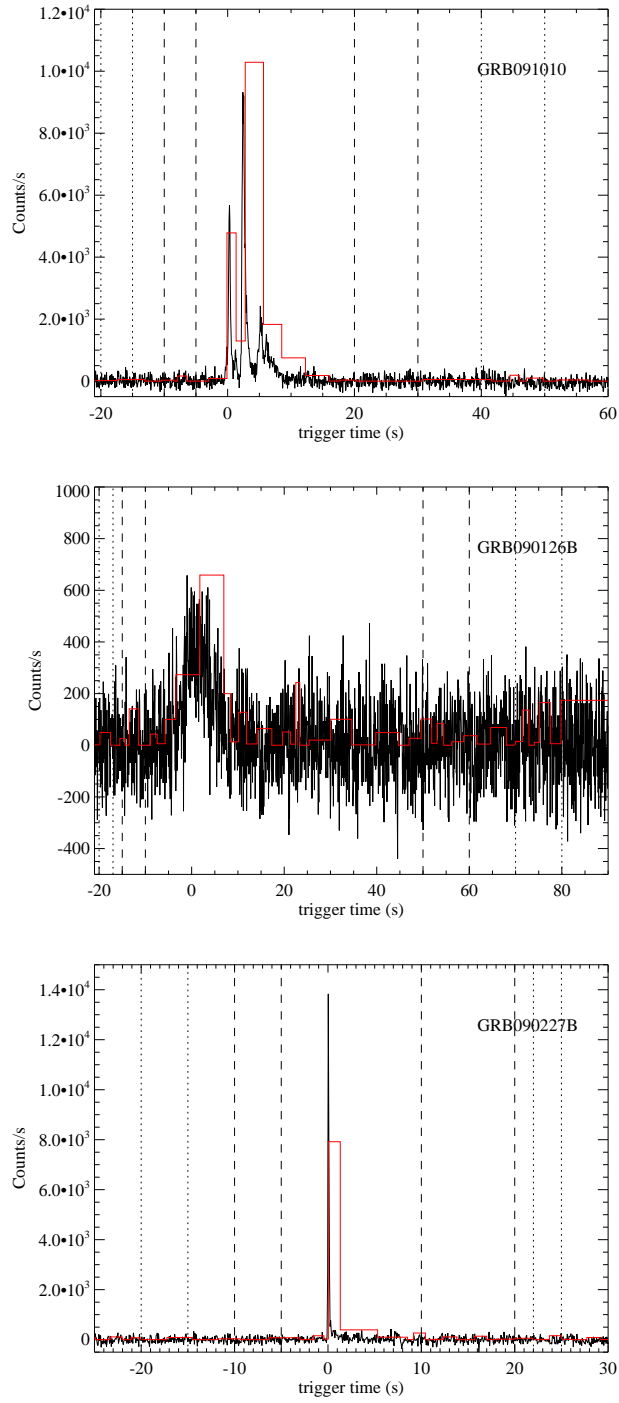


Fig. 1.— Illustrations of background selections (dashed and dotted lines) and the Bayesian blacks (solid lines) for a bright burst (GRB 090910), a weak burst (GRB 090126B), and a short burst (GRB 090227B).

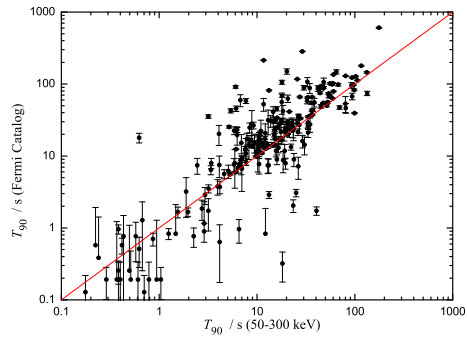


Fig. 2.— Comparison of the derived T_{90} from our method to that reported in the first GBM Catalog (Paciesas et al. 2012) in the 50-300 keV band. The line is the equality line.

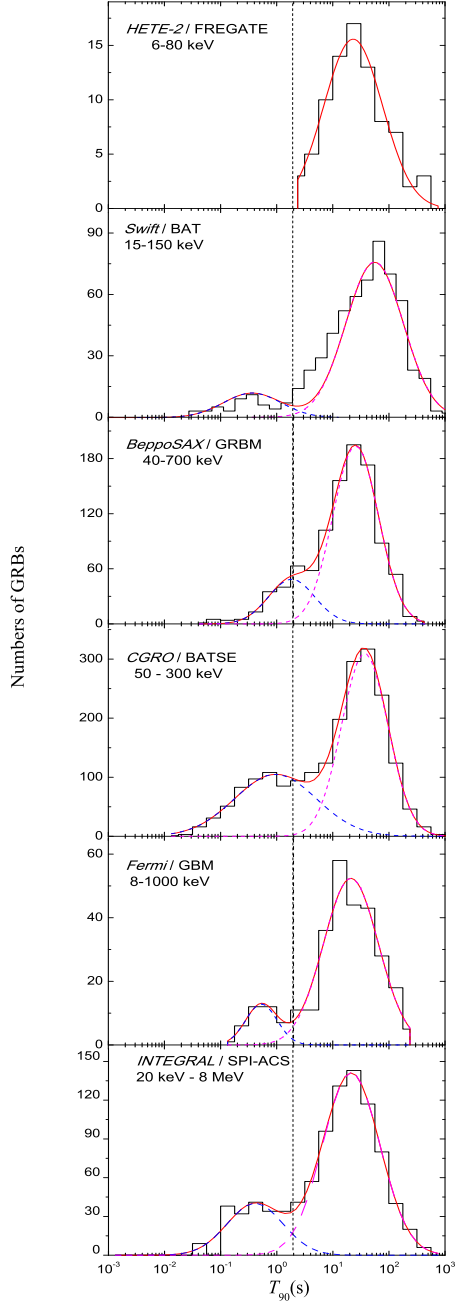


Fig. 3.— Comparison of the T_{90} distributions observed with different instruments. The data of *HETE-2*/FREGATE, *BeppoSAX*/GRBM, CGRO/BATSE, *Swift*/BAT, *INTEGRAL*/SPI-ACS, are taken from Pélangeon et al. (2008), Frontera et al.(2009), Paciasas et al. (1999), Sakamoto et al. (2011), and Savchenko et al. (2012) respectively. The vertical dotted line marks $T_{90} = 2$ seconds. The fits to the distributions with two Gaussian functions or one Gaussian function are also shown.

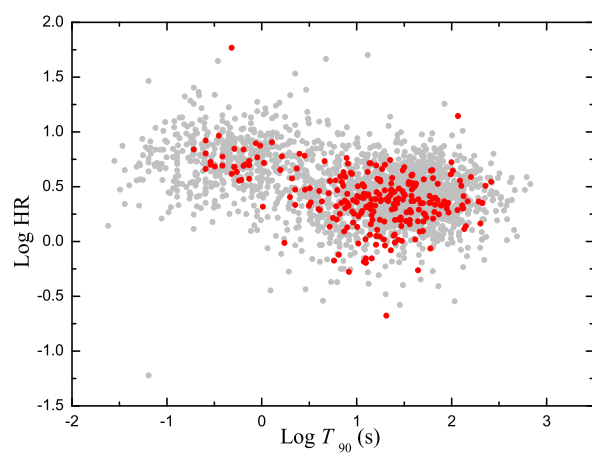


Fig. 4.— The hardness ratio defined with the fluence in the 100-350 keV band to that in the 50-100 keV band as a function of T_{90} for GBM (red) and BATSE (gray) GRBs.

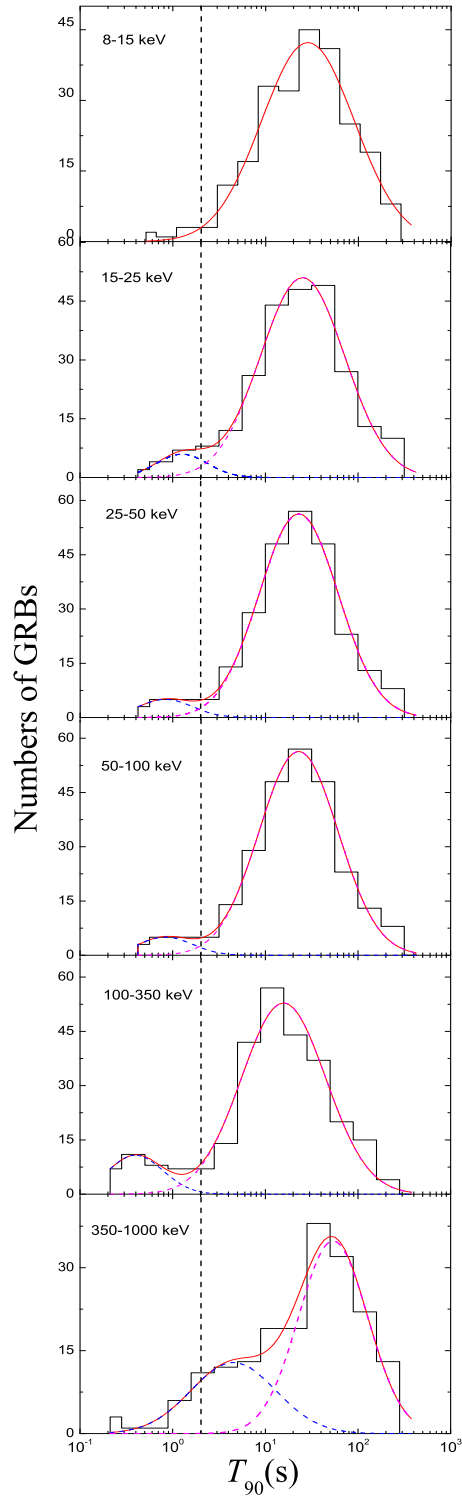


Fig. 5.— T_{90} distributions in different energy bands. The dotted line corresponds to $T_{90} = 2$ seconds. The fits with a model of two log-normal function are also shown (dashed and dotted lines).

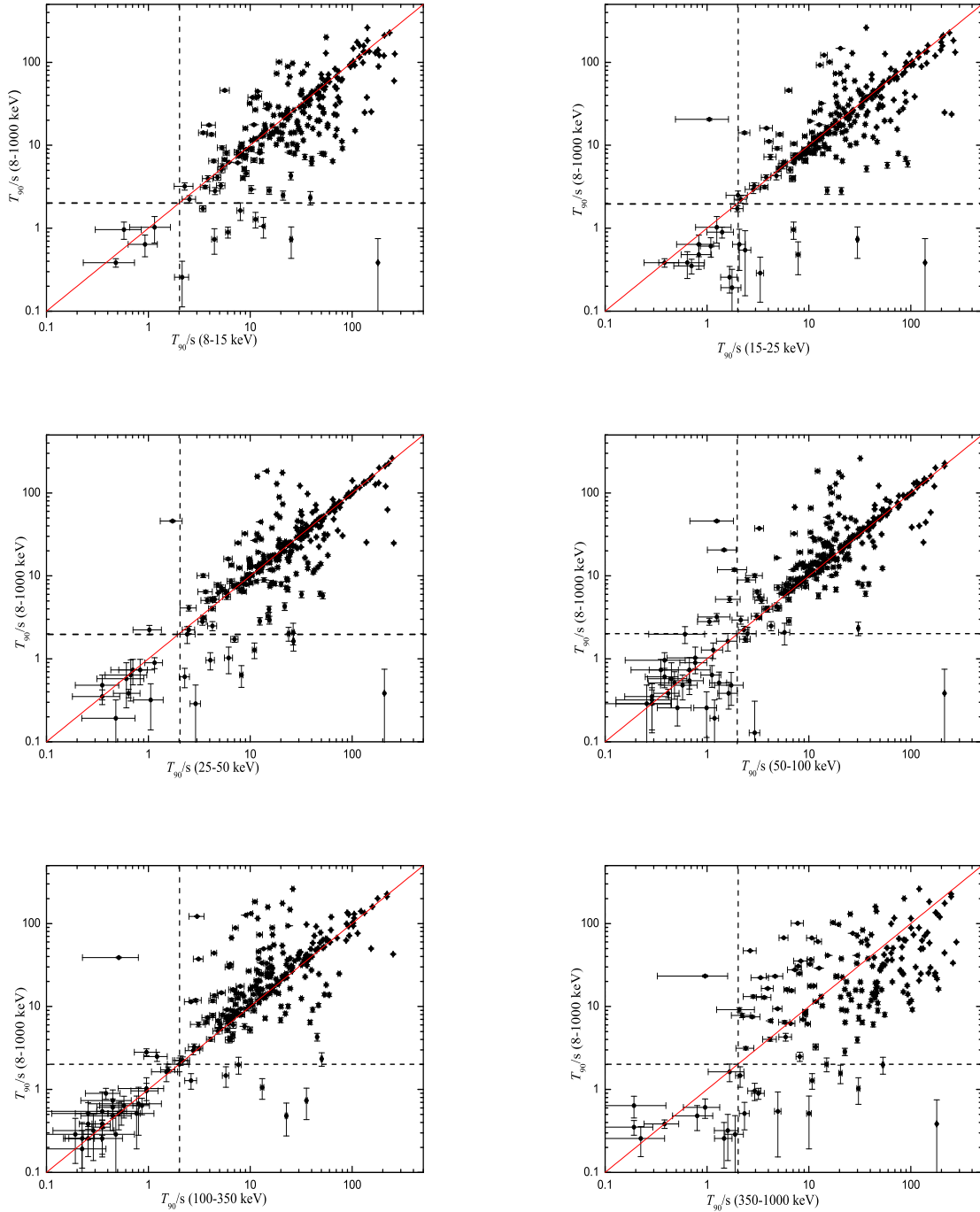


Fig. 6.— Comparisons between T_{90} measured in the 8-1000 keV energy band and some sub-energy-band. The dotted line denotes $T_{90} = 2$ seconds and the solid lines are the equality line.

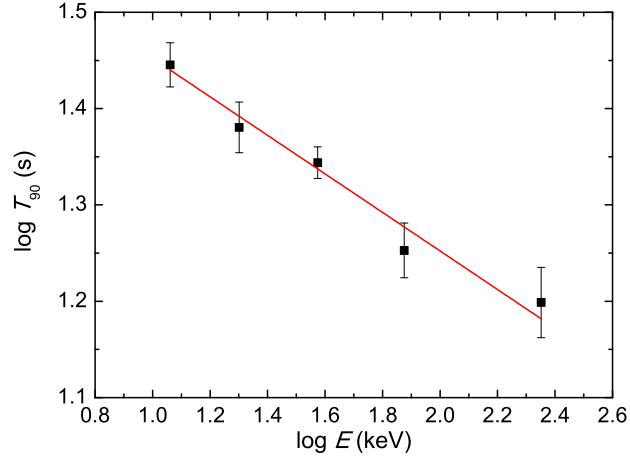


Fig. 7.— Energy dependence of T_{90} for the LGBRs in our sample. The solid line is the best fit to the data.

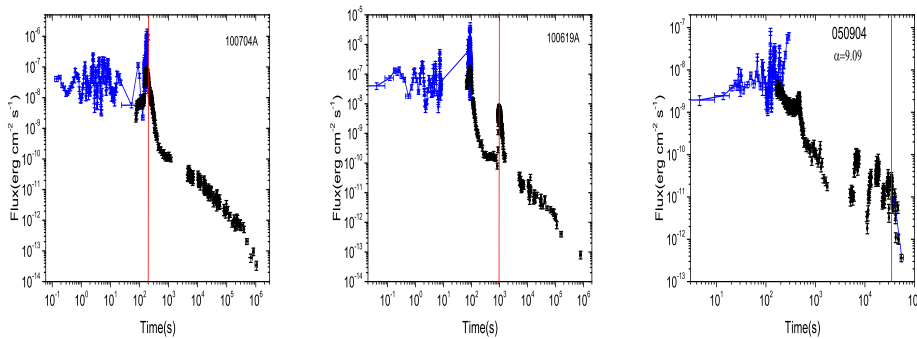


Fig. 8.— Examples of XRT light curves without (*left panel*) or with (*middle and right panels*) significant flares after T_{90} . The connected data points are the extrapolation of the BAT data to the XRT energy band. Vertical lines correspond to the peak of last X-ray flare, which is used to define the total central engine time scale T_f .

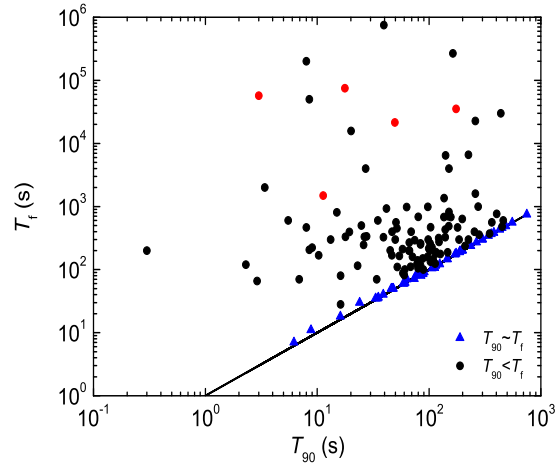


Fig. 9.— The total central engine time scale (T_f) that is defined with the peak time of the last X-ray flare as a function of T_{90} for our *Swift* GRB sample. The triangles denote the GRBs whose $T_{90} \sim T_f$ and the solid dots are for those GRBs with $T_f > T_{90}$. The solid red dots are the GRBs that their X-ray emission is dominated by flares. The line is the equality line.